ACS OMEGA

Open Access



http://pubs.acs.org/journal/acsodf

Article

# Bioinspired High-Strength Borate Cross-Linked Microfibrillated Cellulose Composite Laminate with Self-Extinguishing Flame Retardance and Superhydrophobicity for Self-Cleaning

Huajie Shen,* Xinyuan Zheng, Liangzhou Dong, and Donghai Huang

Cite This: *ACS Omega* 2023, 8, 41458−41468

Read Online

ACCESS | Metrics & More | Article Recommendations | Supporting Information

**ABSTRACT:** The cross-linking of borates enhances the intercellular structural connection, resulting in the creation of a mechanically superior structural material composed of lignocellulose and borate. This is accomplished by employing a mechanical pretreatment procedure and a binder-free hot-pressing method. Nevertheless, these materials frequently encounter constraints in humid environments, making it challenging to simultaneously achieve the desired performance objectives. Here, the prepressed bulk of microfibrillated cellulose is modified and subjected to hot pressing, while ensuring that the enhanced physical and mechanical properties of lignocellulosic recombinant materials are maintained. This modified material is termed the microfibrillated cellulose composite laminate (MCCL). These findings indicate that the application of compression, shear, and friction forces during hot-pressing results in the formation of a compact laminated structure using pine lignocellulose. The self-cleaning MCCL exhibits significantly improved mechanical properties compared with untreated lignocellulose materials (ULM). Specifically, the flexural strength (MOR), modulus of elasticity (MOE), and internal bonding strength (IB) of self-cleaning MCCL are found to be 5 times, 2.5 times, and 4.1 times higher, respectively, than those of ULM. This improvement in the pine lignocellulose can be attributed to the enhanced layering and branching that occurs during mechanical milling. This results in a higher proportion of ester and hydrogen bonds, as well as an increased exposure of hydroxyl groups. As a result, the modified MCCL exhibits self-cleaning properties, as evidenced by its surface water contact angle (WCA) of 152°. The rolling/jumping water droplets, which contain pollutants, effectively remove graphite powder from the surface, leaving it clean. Moreover, MCCL demonstrates exceptional dimensional stability and flame-retardant self-extinguishing properties, making it highly promising as a structural material in engineering technology.


## 1. INTRODUCTION

Wood is a complex organism[1] with a strong cell wall that allows it to function as a larger organism.[2] The cell wall is composed of several components, including cellulose, hemicellulose, and lignin.[3,4] Each of these components has a precise composition and structure, with features such as tiny openings, membranes, and laminar walls.[1] Lignin plays a role in binding the cellulose and hemicellulose cells together, while borate connections create and reinforce the network between cells.[5,6] Additionally, wood contains low levels of boronic acid cross-linked polysaccharide rhamnogalacturonan II,[7,8] which further strengthens and stabilizes the cell wall.[7] This improves the mechanical of wood support and resistance to gravity and strong lateral forces.[9] The boronic acid ion exhibits the ability to covalently bond with oxygen-containing functional groups in various environments. As a result, it serves as an effective cross-linker for higher plants and an essential nutrient for all healthy plants.[10−12] Building upon the concept of borate cross-linking in vegetation,[13,14] researchers have investigated the self-bonding cross-linking between borates and graphene nanosheets, which greatly enhances the mechanical properties and survival capabilities of plants.[15,16] Additionally, borates are known for their nontoxicity, high reactivity, nonflammability, and noncorrosiveness. They also possess antibacterial and antifungal properties.[17] These admirable attributes make borates a promising choice for the development of binderless lignocellulose composites.

Microfibrillated cellulose, which is a type of nanolignocellulose found in wood, is extensively utilized due to its abundant high performance.[14,18,19] Lignocellulose, the main source of microfibrillated cellulose, can be derived from various sources such as agricultural waste, forestry waste, processing residues, and domestic waste.[20,21] These sources primarily consist of crop residues and livestock,[22] forestry "three residues" and waste woody materials,[23] agricultural processing waste, industrial processing waste,[24] and urban domestic waste resources.[25] The sustainability aspect of microfibrillated

Received: July 20, 2023
Accepted: October 5, 2023
Published: October 23, 2023

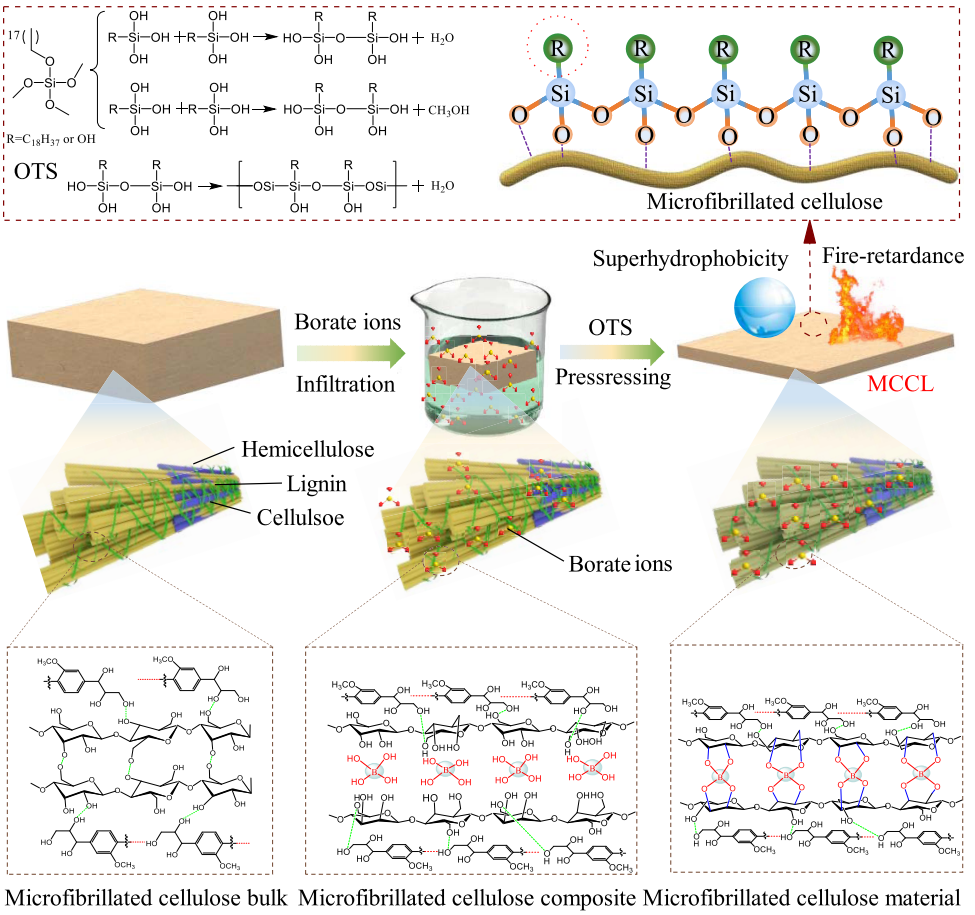


**Figure 1.** Schematic of stable covalent cross-linking structure and nanolignocellulose/borate cross-linking interconnected cell wall in Pine lignocellulose, as well as the hydrolysis mechanism of the OTS on the surface of microfibrillated cellulose.

cellulose, which is obtained from the utilization of waste resources, has attracted attention because it offers a potential alternative to synthetic materials by converting waste resources into valuable biomass resources.[21,26] The development and exploitation of lignocellulose-based materials hold great promise in alleviating resource constraints, reducing environmental impact, improving living standards, and driving economic growth.[19] This development is crucial in maintaining ecological balance, advancing biomass energy, and utilizing waste resources to combat environmental pollution and promote the use of renewable energy sources.[27] Therefore, considering sustainability concerns, strategic research efforts are needed to focus on the development of renewable energy and achieving rapid and significant advancements. Currently, several processing and synthesis techniques, such as Langmuir−Blodgett, knockdown, nanocombination, and strain release, as well as top-down strategies, have successfully been utilized in the preparation of three-dimensional bulk nanocomposites. However, the mechanical strength, particularly in terms of bending strength and toughness, may still be limited due to the insufficient design and control of micro-nano interfaces in biomimetic nanocomposites. Additionally, structural materials derived from biological resources, which aim for sustainability, are prone to water and moisture absorption as well as mold and decay, owing to the abundance of hydroxyl groups. Therefore, it is crucial to consider the stability of these materials in harsh environments, such as water, acids, and bases.

To address the issue of inadequate adhesion in microfibrillated cellulose laminates without the use of a binding agent, we have employed a cross-linking method inspired by higher plants that utilize borate ions. This method involves a mechanical hot-rubber milling process and a binder-free hot-pressing technique, resulting in the production of a high-strength structural lignocellulose-based composite (Figure 1). This composite possesses self-extinguishing flame retardancy and superhydrophobic self-cleaning properties. The microfibrillated cellulose composite laminate (MCCL) demonstrates a compact laminated structure with a low density (0.86 g/cm$^3$), high modulus, and excellent environmental stability. Additionally, it shows self-extinguishing flame retardancy and superhydrophobic self-cleaning properties, as evidenced by a water contact angle (WCA) measurement of 152°.

## 2. RESULTS AND DISCUSSION

### 2.1. Structural and Morphological Characterization.

Figure 1 presents a visual representation of the sequential steps involved in the fabrication of MCCL via binderless hot-pressing. The process includes three stages: swelling, colloidal milling, and binderless hot-pressing. It is important to note that during this process, a network is formed between the nanolignocellulose and borate, resulting in cross-linking between the two polysaccharides. Figure 2a shows untreated lignocellulose, which has a slender and polished appearance. Upon closer inspection at high magnification (Figure 2a, inset), noticeable pits can be observed. Figure 2b provides a



https://doi.org/10.1021/acsomega.3c05251
ACS Omega 2023, 8, 41458−41468

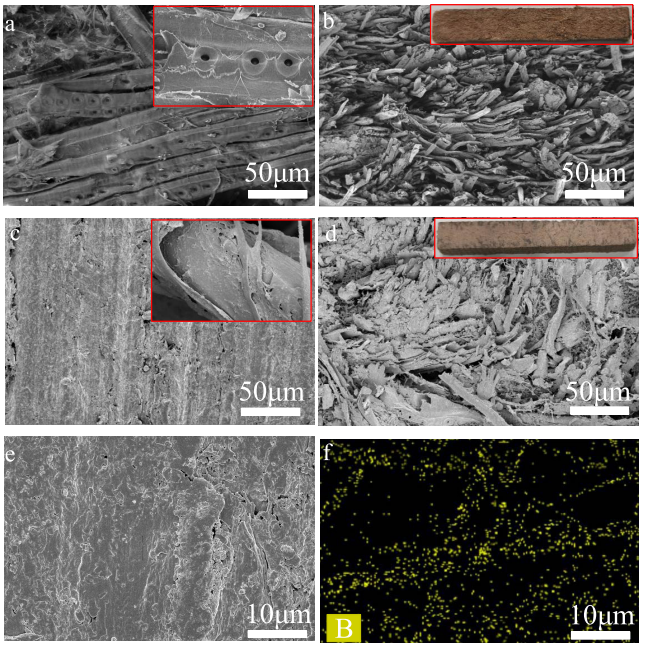


**Figure 2.** (a) SEM image of untreated lignocellulose. (b) SEM image of the cross section of binderless hot-pressed ULM. (c) SEM image of microfibrillated cellulose by mechanical hot rubber milling. (d) SEM image of the cross section of the binderless hot-pressed MCCL. (e) SEM image of the surface of MCCL. (f) Sectional energy-dispersive X-ray spectroscopic (EDS) elemental distribution of element B in (e).

macroscopic and microscopic view of the cross-sectional morphology of binderless hot-pressed ULM. It can be observed that ULM consists of slender strips of pine lignocellulose that are intertwined in a disordered manner. Figure 2c depicts the micromorphology of the microfibrillated cellulose produced through mechanical hot-rubber milling. It is evident from Figure 2c that the microfibrillated cellulose exhibits a distinct dense layering structure. This cross-linking of molecular chains of microfibrillated cellulose resulted in the formation of a dense stratified structure, as seen in the macroscopic and microscopic morphologies of the MCCL (Figure 2d). The mechanical milling of untreated lignocellulose using a colloid mill produced compressive, shear, and friction forces, leading to the generation of a laminar structure in pine lignocellulose. Under high magnification (Figure 2e,f), effective binding of the microfibrillated cellulose of self-cleaning MCCL with boric acid can be observed, which is reflected by the formation of covalent bonds between the −OH groups of the polysaccharides and boric acid during the hot pressing process.

**2.2. Characteristics of Self-Cleaning MCCL.** Figure 3a displays the XRD spectra of the ULM, MCCL, and self-cleaning MCCL. The XRD spectrum of the ULM shows no distinct characteristic peaks, except for the cellulose peaks at 16 and 22°. These peaks correspond to the (110) and (002) reflective surfaces of pine lignocellulose. The XRD spectrum of the MCCL shows no significant differences compared to that of the ULM, except for an increase in relative crystallinity. The observed XRD peaks align with the increase in relative crystallinity, apart from the increase in relative crystallinity of the characteristic cellulose characteristic peaks. The results suggest that the MCCL exhibits high phase purity, consisting of only pine nanolignocellulose products and the products after hydroxymethylation.

The chemical structure characteristics of ULM, MCCL, and self-cleaning MCCL were investigated by using Fourier transform infrared (FTIR) spectroscopy. Figure 3b shows that the FTIR spectra of MCCL and self-cleaning MCCL were generally similar to those of ULM, indicating minimal changes in the overall chemical composition. However, notable alterations were observed in the absorption bands of MCCL at 1100−1230, 1700−1725, and 3650−3200 $cm^{-1}$. The FTIR spectra of the self-cleaning MCCL exhibited similarities to those of MCCL, suggesting that the mechanical and hot-rubber milling processes did not destroy the chemical composition of the lignocellulose and that the characteristics of the lignocellulose are well preserved. A comparison of the FTIR spectra of the MCCL and self-cleaning MCCL reveals that the broad peak at 3440 $cm^{-1}$ corresponds to the tensile vibration peak of hydroxyl (−OH), which indicates the occurrence of −OH bonds during rubber milling. The tensile vibration peak at 2908 $cm^{-1}$ is characteristic of C−H in cellulose. The absorption peak at 2300 $cm^{-1}$ disappears in the self-cleaning MCCL due to the large force constants of the contained hydrogen atom bonds (C−H and O−H) and the heavy bond (C−O). The vibrations of these bonds are affected by the other parts of the molecule. The peak observed at 1430 $cm^{-1}$ corresponds to the bending vibration of $CH_2$ in lignin and polysaccharides, whereas the peak at 1385 $cm^{-1}$ is attributed to the bending vibration of C−H in cellulose and hemicellulose. Additionally, the peak at 1747 $cm^{-1}$ represents the stretching and vibration of the aromatic ring's C═C, which suggests the presence of lignin. The absorption peak at 1230 $cm^{-1}$ was amplified due to the presence of lignin; a phenolic substance formed during the mechanical rubber grinding process. Furthermore, absorption peaks correspond-

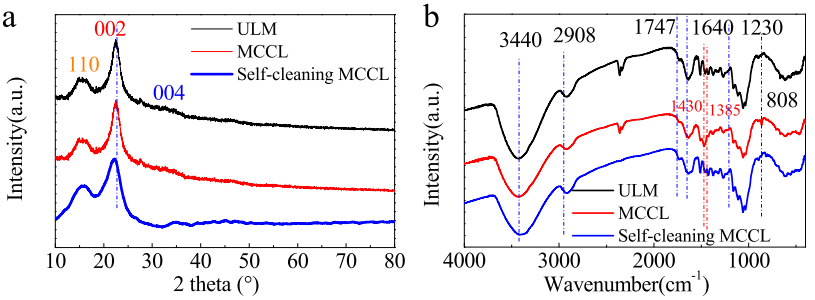


**Figure 3.** (a) XRD patterns of ULM, MCCL, and self-cleaning MCCL, respectively. (b) FTIR patterns of ULM, MCCL, and self-cleaning MCCL, respectively.



https://doi.org/10.1021/acsomega.3c05251
ACS Omega 2023, 8, 41458−41468

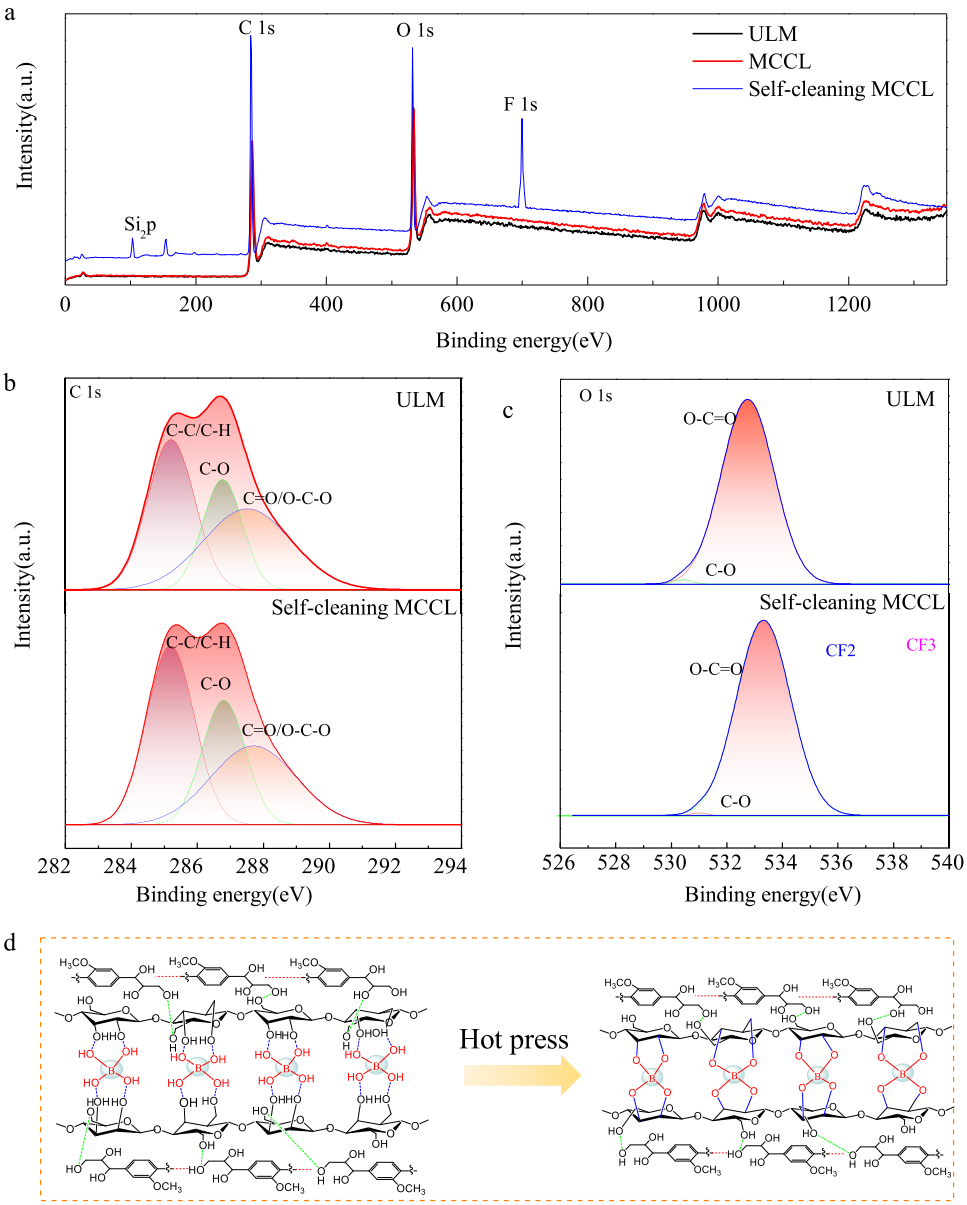


**Figure 4.** (a) Survey XPS of ULM, MCCL, and self-cleaning MCCL. (b) C 1s (b) and (c) O 1s of ULM and self-cleaning MCCL (F 1s), respectively. (d) Schematic illustration of the formation of the borate cross-linked network between two adjacent polysaccharides (Left: Formation of hydrogen bonds; right: hot pressing inducing the formation of covalent bonds).

ing to C═O bonds were observed at 1698 and 574 $cm^{-1}$, respectively. The stretching vibrations of C−F groups in the self-cleaning MCCL were observed in the range 1350−1180 $cm^{-1}$. Additionally, the absorption peaks at 803 $cm^{-1}$ were primarily attributed to the stretching vibration of the Si−O and Si−$CH_3$ bands. These results conclusively demonstrate that the self-cleaning MCCL maintains its original chemical composition and retains active hydroxyl groups. These hydroxyl groups are formed by the condensation reaction of borate orthoester formation and furfural resin adhesive. The presence of these active hydroxyl groups supports the reaction mechanism depicted in Figure 1, which involves the formation of both hydrogen and covalent bonds.

The surface atomic composition and chemical bonding of ULM, MCCL, and self-cleaning MCCL are depicted in Figure 4. The low-resolution survey spectra of these specimens are shown in Figure 4a. A comparison reveals that the primary chemical composition of the microfibrillated cellulose remained unchanged and consisted mainly of C, H, and O elements, which can be observed at energies of 285.69 and 532.67 eV. Figure 4b displays the spectral peaks of C 1s for the ULM and self-cleaning MCCL. The three small peaks within the overall contour were obtained through peak decomposition, and the overall contour closely matched the synthetic curves of these peaks, indicating a precise fitting. The absence of C4 in the C 1s spectrum peak can be attributed to the colloidal nature of self-cleaning MCCL, which contains a minimal number of carboxylic acid groups. Additionally, it is worth noting that the surface photoelectron spectrometer employed in this study may have a relatively low resolution. The detection of three minor peaks suggests the existence of carbon atoms in different chemical structures, namely, C1, C2, and C3. The milling process led to a substantial decrease in the quantity of C−C bonds, and a noticeable increase in the


https://doi.org/10.1021/acsomega.3c05251
ACS Omega 2023, 8, 41458−41468

**Table 1. Element Content and O/C Ratios of the ULM and Self-Cleaning MCCL**

| | peak position (eV) | | | peak area (%) | | |
|---|---|---|---|---|---|---|
| specimen | C1 | C2 | C3 | C1 | C2 | C3 |
| ULM | 285.21 | 286.76 | 287.52 | 37.98 | 23.58 | 38.45 |
| self-cleaning MCCL | 285.18 | 286.80 | 287.69 | 35.32 | 26.08 | 38.60 |

| | peak position (eV) | | peak area (%) | | |
|---|---|---|---|---|---|
| specimen | O1 | O2 | O1 | O2 | nO2/nO1 |
| ULM | 533.25 | 531.27 | 99.91 | 0.09 | 0.0009 |
| self-cleaning MCCL | 533.31 | 531.01 | 99.62 | 0.38 | 0.0038 |

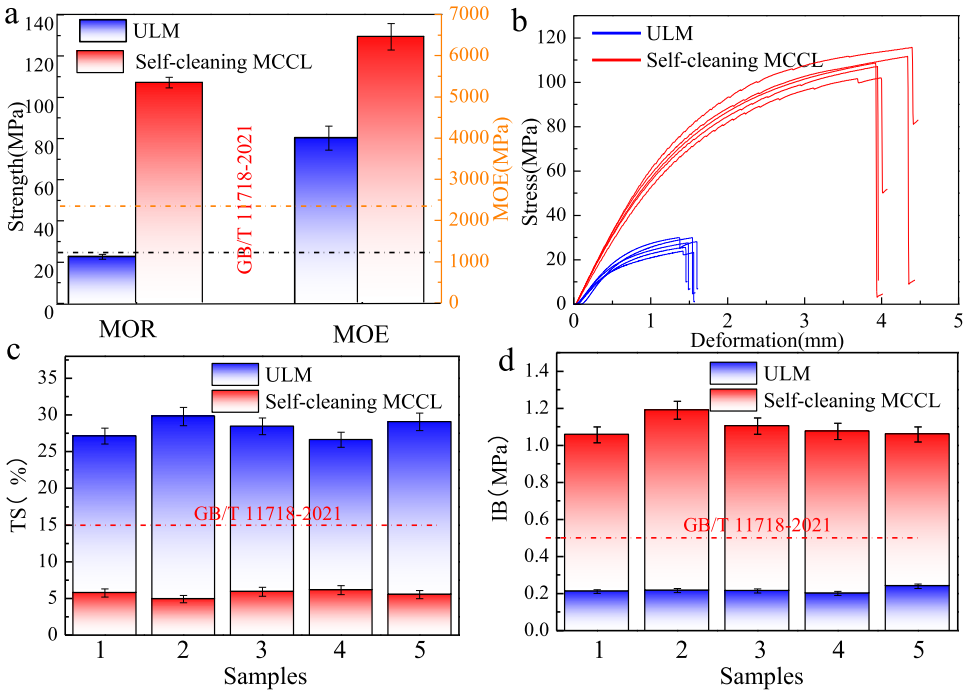


**Figure 5.** Mechanical strength histogram (a), stress−deformation curves (b), TS (c), and IB (d) of ULM and self-cleaning MCCL.

amount of C3, which suggests the formation of numerous oxygen-containing functional groups on the self-cleaning MCCL surface.

The O2 content in ULM is low, while its content of O1 is high, indicating that surface oxygen and carbon in ULM primarily form cross-links via a C−O single bond, with less oxygen forming double bonds linked to carbon. In contrast, the self-cleaning MCCL exhibits an increase in the level of the O2 content and a decrease in the level of the O1 content, indicating a shift in the oxidation state of carbon. Table 1 presents the C/O element values and the percentages of C and O in diverse chemical states. The increase in the oxidation state of carbon in the self-cleaning MCCL is supported by the higher O2/O1 ratio. The elevated O2 peak observed can be attributed to the increased presence of carbonyl groups resulting from the oxidation and condensation reaction of lignin during the milling procedure. Conversely, the decrease in the peak area of O1 can be attributed to the drying out of the microfibrillated cellulose component and the degeneration of hemicellulose, both of which lead to higher oxygen content in the ULM. Additionally, the results presented in Table 1 suggest that the highest ratio of nO2/nO1 was obtained with the milling pretreatment, demonstrating the higher concentration of C═O content in the ULM. The XPS supports the findings of the FTIR spectra, demonstrating that boric acid effectively forms a covalent bond with the −OH groups of the polysaccharides, as depicted in Figure 1. The peak at 103.53 eV in the Si 2p spectrum of self-cleaning MCCL is attributed to the presence of Si−O and Si−C groups. This is evidenced by the appearance of new silica peaks (Si 2s and Si 2p) in addition to carbon and oxygen peaks after modification with the OTS (Figure 4a). The overall spectrum of the modified self-cleaning MCCL sample indicates that the Si elements, mainly derived from the OTS treatment solution, were primarily responsible for fluorination of the surface of microfibrillated cellulose (Figure 4c). Therefore, despite the modification with OTS, the microfibrillated cellulose retained its low surface energy properties and maintained superhydrophobicity, even when the original test solution was altered. This can be attributed to the robust covalent cross-linking structure, which was achieved through the combination of nanolignocellulose/borate cross-linking and the covalent bonding with boric acid to the −OH groups of the polysaccharides, as demonstrated in Figure 4d. The stable covalent cross-linked structure, along with synergistic hydrogen bonding, contributes to the exceptional bonding strength and water resistance of the adhesive fabricated from microfibrillated cellulose.

**2.3. Mechanical Properties Characterization.** The results of the flexural strength (MOR) and modulus of elasticity (MOE) analysis are depicted in Figure 5a, comparing



https://doi.org/10.1021/acsomega.3c05251
ACS Omega 2023, 8, 41458−41468

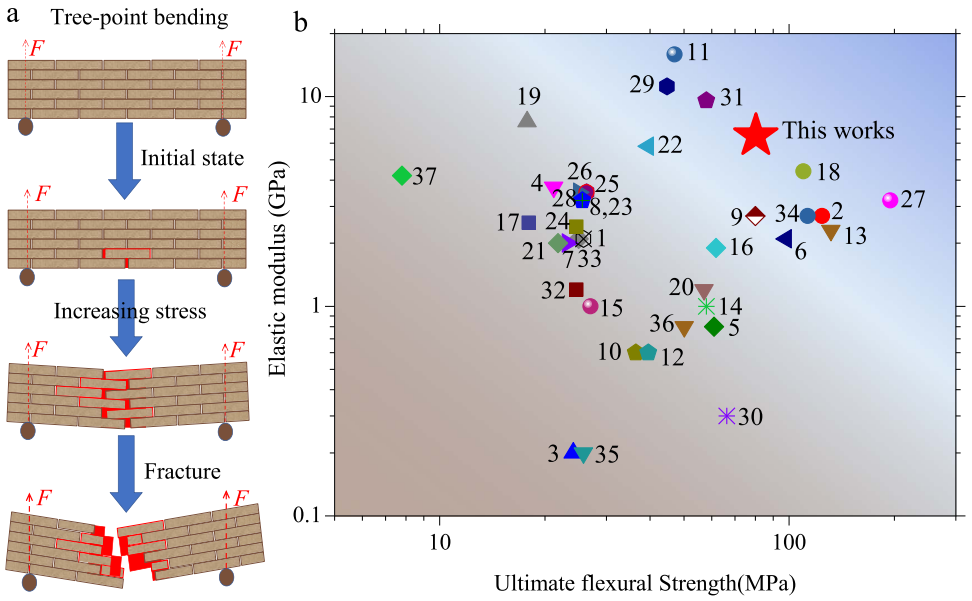


**Figure 6.** (a) Proposed synergistic mechanism of the self-cleaning MCCL. (b) Ashby diagram of ultimate flexural strength and elastic modulus for the self-cleaning MCCL and various natural and artificial composites (Table S1).

the ULM and self-cleaning MCCL. The self-cleaning MCCL exhibits an MOR of 107.27 MPa and an MOE of 6498 MPa, which are 5 times and 2.5 times higher than the ULM, respectively. Furthermore, it exceeds the Chinese national standard No. GB/T11718−2021 by 2.5 times and 2.7 times. The stress−displacement curves of the ULM and self-cleaning MCCL are depicted in Figure 5b. The average maximum loads for the two specimens are 21.44 and 115.27 N, respectively, with the self-cleaning MCCL exhibiting the highest MOR. The mechanical performance of the self-cleaning MCCL is superior to that of the ULM and meets the relevant standards of GB/T11718−2021. The self-cleaning MCCL demonstrates a higher internal bond strength (IB) value of 0.880 MPa, which is 4.1 times higher than the relevant standards of GB/T11718−2021 and 1.8 times higher than the ULM (Figure 5d). In contrast, its thickness expansion rate of water absorbing (TS) value is only 5.66%, which is significantly lower compared to that of the ULM, showing a 298% reduction (Figure 5c). This difference can be attributed to the mechanical milling processes that resulted in the layering and branching of pine lignocellulose. These processes led to an increase in ester and hydrogen bonds, exposed hydroxyl groups, and cross-linking degree between borate and lignocellulose. The results suggest that the self-cleaning MCCL demonstrates superior mechanical performance compared to the ULM and relevant criteria of the standard GB/T11718−2021, as well as other biomass materials.

Figure 6a illustrates a simplified schematic of the quasi-static three-point bending test conducted on the self-cleaning MCCL. The microfibrillated cellulose constituents are arranged in an alternating pattern. During the three-point bending test, sliding and cracking occur within the self-cleaning MCCL, potentially resulting in the displacement of microfibrillated cellulose elements. Ultimately, the self-cleaning MCCL fails due to the fracture of the microfibrillated cellulose building blocks. Interestingly, the hydrogen bonding between the microfibrillated cellulose building blocks and the laminated structure of the self-cleaning MCCL leads to a synergistic effect (Figure 6a). Conversely, borate cross-linked microfibrillated cellulose demonstrates a brittle behavior under tension because it lacks the ability to regenerate covalent bonds once they are broken. Figure 6b and Table S1 present a comparison of the mechanical properties of the self-cleaning MCCL with lignocellulose-based matrix composites. It is evident from the data that the self-cleaning MCCL demonstrates a superior ultimate MOR and MOE, highlighting its potential suitability for applications requiring high specific strength. In contrast, other materials such as lignocellulose-based composites, wood fiber-based composites, plexiglass, inorganic composite materials, and nacre exhibit poor mechanical stability. Therefore, the results suggest that the self-cleaning MCCL outperforms many natural and wood fiber/lignocellulose-based composite materials in terms of mechanical performance.

**2.4. Self-Extinguishing Flame-Retardant Performance of Self-Cleaning MCCL.** In addition to its exceptional mechanical properties, the self-cleaning MCCL also demonstrates remarkable flame retardancy and self-extinguishing properties. Combustion tests reveal that the UCM quickly spreads and burns under the flame of a butane torch with nearly half of it burned after 240 s (Figure 7a). In contrast, the MCCL showed no significant spreading even after 240 s of exposure to the flame, thanks to its flame-retardant and self-extinguishing characteristics. This demonstrates the exceptionally high flame retardancy of the MCCL (Figure 7b). Furthermore, the self-cleaning MCCL, with its compact stacked microfibrillated cellulose laminate structure, also possesses excellent flame retardancy due to its compact stacked laminate structure (Figure 7c). When the UCM (Figure 7d), MCCL (Figure 7e), and self-cleaning MCCL (Figure 7f) specimens were ignited for 10 s, the specimens were promptly removed from the flame. Although the UCM continued to burn, the flames of MCCL and self-cleaning MCCL were rapidly extinguished, indicating their self-extinguishing properties (Figure 7d−f). This self-extinguishing behavior of the self-cleaning MCCL can be attributed to the compact laminated structure, which reduces its permeability. This structure also facilitates the formation of a protective insulating charcoal layer on the self-cleaning MCCL surface.


https://doi.org/10.1021/acsomega.3c05251
ACS Omega 2023, 8, 41458−41468

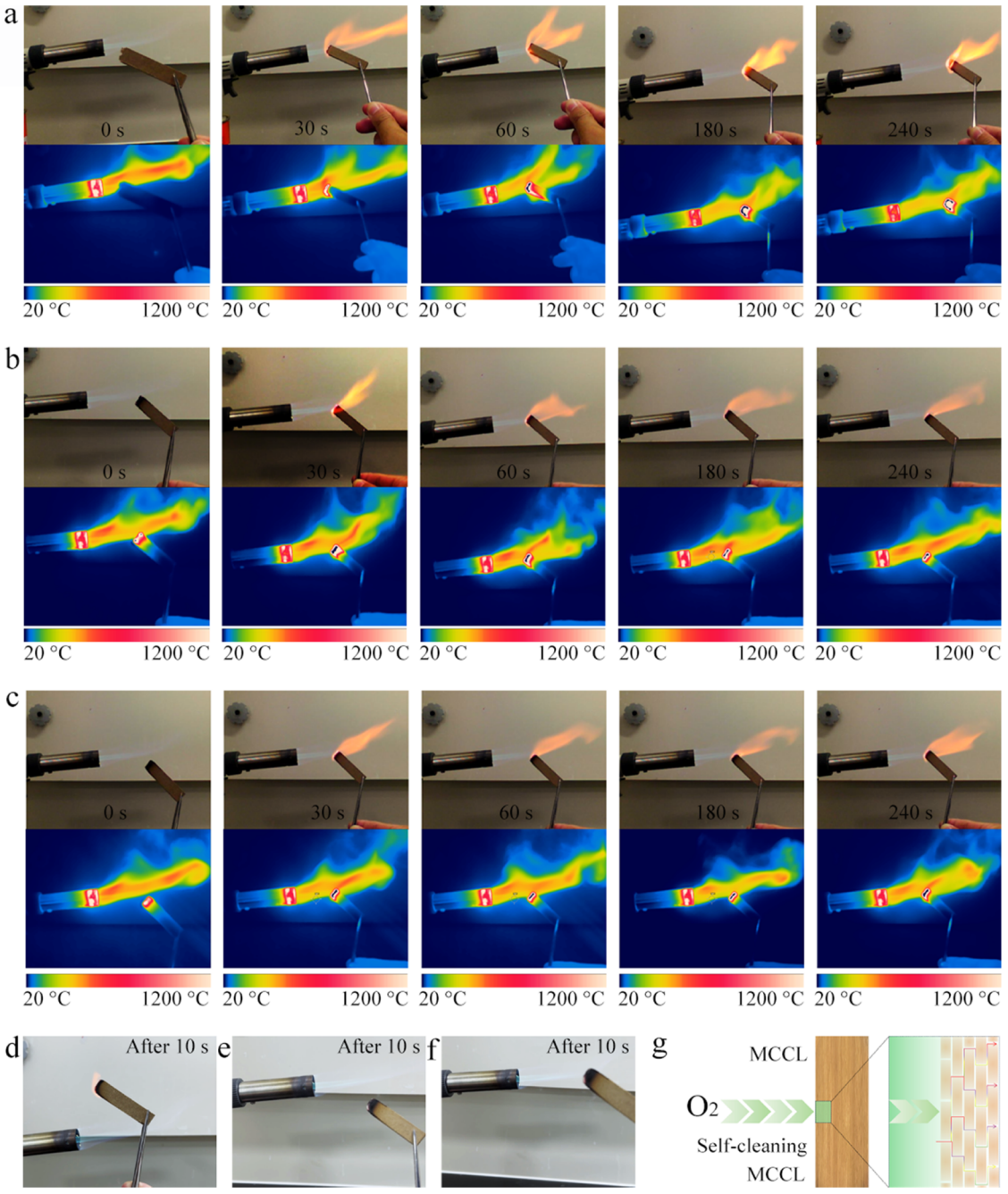


**Figure 7.** Flame-retardant self-extinguishing properties of self-cleaning MCCL. (a) Optical images and infrared pseudocolor map of the flame spread rapidly throughout the UCM within 30 s. (b) Optical images and infrared pseudocolor map of no significant flame spread throughout the MCCL within 240 s. (c) Optical images and infrared pseudocolor map of no significant flame spread throughout the self-cleaning MCCL within 240 s. (d) Continuation of burning behavior of UCM. (e) Self-extinguishing behavior of MCCL. (f) Self-extinguishing behavior of a self-cleaning MCCL. (g) Schematic diagram of the principle of high fire-retardant performance of UCM and self-cleaning MCCL, markedly extending the oxygen transport path to the internal material surface, resulting in high fire-retardant performance.

This dense charcoal layer reduces the diffusion of heat and oxygen, thereby slowing down the rate of heat release and inhibiting combustion reactions. Figure 7g provides a possible explanation for the fire-retardant performance of the self-cleaning MCCL. The densification process plays a crucial role in creating a compact laminated structure of microfibrillated cellulose, which not only reduces the permeability of the self-cleaning MCCL but also inhibits the diffusion of heat. This compact laminated structure greatly lengthens the pathway for oxygen conduction from the external atmosphere to the interior, hence significantly reducing the likelihood of the internal sample coming into contact with oxygen and making it difficult to ignite. Moreover, the stacked layers indicate the formation of an insulating carbon layer during the combustion process. This layer effectively maintains the stability of the overall microstructure when exposed to flames. Consequently, the self-cleaning MCCL with microfibrillated cellulose laminated structure exhibits a relatively low temperature internally, a minimal probability of direct oxygen due to the extended oxygen conduction pathway, and the protective


https://doi.org/10.1021/acsomega.3c05251
ACS Omega 2023, 8, 41458−41468

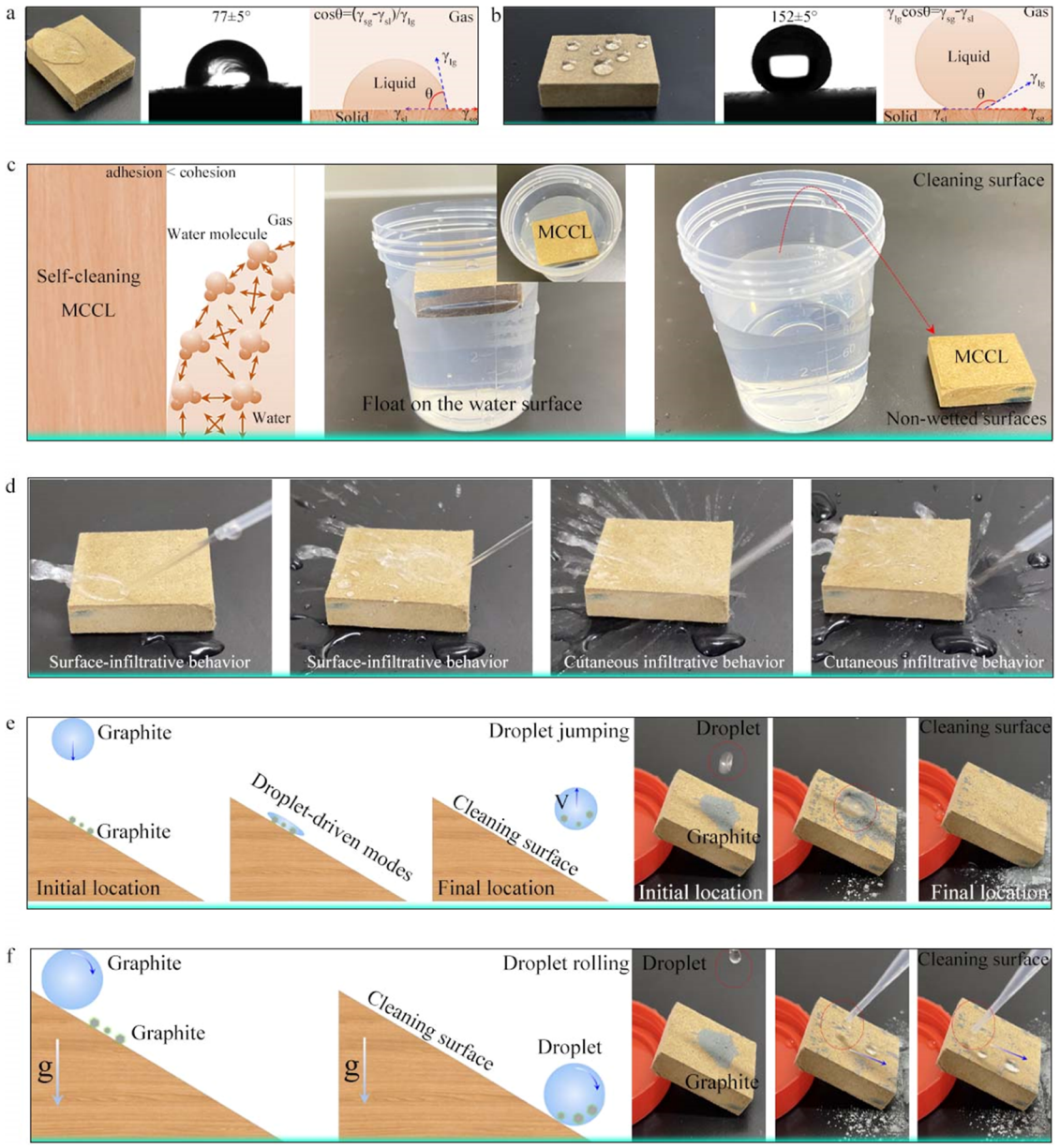


**Figure 8.** Self-cleaning superhydrophobic properties of self-cleaning MCCL. (a) Infiltrative behavior of UCM. (b) Infiltrative behavior of the self-cleaning MCCL. (c) Floating infiltration behavior and nonwetted performance of self-cleaning MCCL. (d) Surface-infiltrative behavior and cutaneous infiltrative behavior of the self-cleaning MCCL. (e) Different modes of surface self-cleaning: coalescence-induced droplet jumping on a self-cleaning MCCL surface. (f) Different modes of surface self-cleaning: coalescence-induced droplet rolling on a self-cleaning MCCL surface.

influence of the insulating charcoal layer, all of which contributing to its high flame retardancy.

**2.5. Wettability Performances.** Figure 8a shows the optical images showing the behavior of water droplets on the ULM surface. It is evident that the WCA of stagnant water droplets on the ULM surface is only approximately 77 ± 5°. This can be attributed to the presence of hydroxyl groups on the microfibrillated cellulose surface, leading to its hydrophilic nature. However, after modifying the surface of microfibrillated cellulose with an octadecyltrichlorosilane (OTS), the WCA value of the self-cleaning MCCL surface significantly increased to 152 ± 5° (Figure 8b). Additionally, the SA measured approximately 6°. These results indicate that the self-cleaning MCCL surface possesses a high WCA and a low SA, effectively preventing water droplets from adhering to it. In general, the higher the hydrophobicity of a solid surface, the larger the WCA. Figure 8a,b demonstrates the sequential increase of hydrophobicity on the self-cleaning MCCL surface from left to right, resulting in a higher WCA compared to the previous state. When the self-cleaning MCCL is tilted at a certain angle (Figure 8a,b), droplets on the hydrophilic MCCL surface slide down simultaneously, whereas this does not occur on the superhydrophobic MCCL surface. This difference highlights the inherent distinction between the static WCA and the dynamic WCA. The dynamic behavior of droplets on MCCL surfaces is typically characterized by sliding, tilting, and pinning, with varying effects on different MCCL surfaces. For instance, the lotus leaf surface exhibits self-cleaning superhydrophobic properties with an extremely small WCA hysteresis, allowing droplets to freely roll on its surface.

When a water drop is placed on a smooth solid surface, such as MCCL, and reaches a state of equilibrium, the surface



https://doi.org/10.1021/acsomega.3c05251
ACS Omega 2023, 8, 41458−41468

tensions at the interfaces of the solid, gas, and liquid phases also reach relative equilibrium. This can be described by the relationship between the solid surface contact angle and the three-phase surface tensions, which is defined by Young's equation

$$\gamma_{SV} = \gamma_{SL} + \gamma_{LV} \cos\theta$$

$$\cos\theta = \frac{\gamma_{SV} - \gamma_{SL}}{\gamma_{LV}}$$

where $\theta$ is the contact angle between the liquid droplet and the solid surface, $\gamma_{SV}$ is the surface free energy at the solid−gas interface, $\gamma_{SL}$ is the interfacial tension at the solid−liquid interface, and $\gamma_{LV}$ is the liquid surface tension at the gas−liquid interface.

At the same time, the surface of the self-cleaning MCCL remains dry after immersion in water due to the ultrahigh water repellency. The building blocks of the self-cleaning MCCL do not absorb water but instead float on the water surface. To determine the float effect induced by the superhydrophobic interface, self-cleaning MCCL was used. Figure 8c illustrates that the self-cleaning MCCL exhibited a surface energy lower than water. Consequently, the water cohesion force on the self-cleaning MCCL was reduced by the superhydrophobic interfaces. The shape of the water surface near the self-cleaning MCCL exhibited a convex meniscus, which indicates that the cohesion forces between the self-cleaning MCCL and water molecules were greater than the adhesion forces among the molecules.

A syringe was utilized to forcefully inject water onto the surface of the self-cleaning MCCL (Figure 8d). The water droplets were repelled, causing them to disperse in different directions as the flow rate increased. Nonetheless, the self-cleaning MCCL surface remained clean and dry, demonstrating its superhydrophobic properties with low adhesion. Similarly, when water was sprayed onto the freshly cut surface of self-cleaning MCCL, the droplets were scattered and repelled, resulting in a clean and dry surface. This confirms the stable low-adhesion superhydrophobic properties of the self-cleaning MCCL, indicating uniformity of the self-cleaning MCCL modification conducted in this study. To further demonstrate the self-cleaning capability of the self-cleaning MCCL, Figure 8e displays the dynamic process of self-cleaning. Graphite, renowned for its high adsorption capacity, was applied onto the surface of the self-cleaning MCCL. Afterward, the contaminated surface was washed with water droplets. Figure 8f effectively demonstrates the facile removal of graphite by the rolling water droplets, resulting in a pristine surface. These findings underscore the lignocellulosic composite surface to combat contamination.

## 3. CONCLUSIONS

A method employing efficient mechanical hot-rubber milling and hot-pressing was utilized to successfully develop a self-cleaning MCCL with exceptional mechanical properties. The results demonstrated that the core layer of the self-cleaning MCCL displayed excellent compactness, thereby significantly improving the MOR and MOE. In comparison to ULM, the self-cleaning MCCL exhibited a 5 times increase in MOR, a 2.4 times increase in MOE, and a 4.1 times increase in IB value, with a 298% decrease in TS value. These exceptional mechanical properties surpass those of ULM and meet the requirements of standard GB/T11718−2021 and other biomass materials. The compact laminated structure of self-cleaning MCCL effectively reduces the permeability of oxygen, thereby enhancing its self-extinguishing flame retardancy in buildings and automobiles. Additionally, it easily forms a protective insulating charcoal layer on its surface, which reduces the diffusion of heat and oxygen. Furthermore, the combination of compact laminated configuration and OTS results in robust superhydrophobicity and excellent self-cleaning properties for the self-cleaning MCCL prepared. It has a WCA of 152 ± 5° and a SA of approximately 6°. Globally, the approach outlined in this study has the potential to be integrated with various inorganic functional materials to create environmentally friendly and sustainable biomaterials. These biobased materials may possess a broad range of supplementary functionalities, such as being lightweight, durable, acoustically, and thermally insulating, as well as exhibiting self-cleaning properties.

## 4. METHODS

**4.1. Materials.** Pinus Yunnanensis Franch (water content: 15%, length: 400−1000 $\mu$m, average diameter: 40 $\mu$m) was purchased from Southwest Timber Market in Kunming, Yunnan Province, China. The cellulose content of Yunnan pine is 55%, hemicellulose is 25%, lignin is 13%, and ash is 7%.

**4.2. Preparation of the Microfibrillated Cellulose Material.** The process of developing microfibrillated cellulose material involved the utilization of pine lignocellulose that was first dried and blended with a fresh sodium borate solution (0.5 M) in deionized water solution in a weight ratio of 39:1 (wt 2.5%). Following this, the pine lignocellulose was subjected to swelling at 60 °C for 1 h before being placed into a colloid mill, where it was subjected to grinding via a rotational speed of 2880 rpm for a duration of 6 h. The resulting homogeneous microfibrillated cellulose glue was then processed to attain a 100% water content. It was then immersed in a 1% OTS ethanol solution for modification. The final step involved the development of the microfibrillated cellulose material through binderless hot-pressing for 30 min (hot pressing temperature 200 °C, pressure 2.5 MPa, thickness 10 mm). Wood is a highly intricate organism that relies on a microscopically robust cell wall in order to attain self-sufficiency as a macroscopic organism. The cell wall consists primarily of lignin, cellulose, and hemicellulose, each with a meticulously structured composition including minute openings, membranes, and laminar walls.

**4.3. Characterization.** The micromorphologies of untreated lignocellulosic specimens and microfibrillated cellulosic materials were analyzed by scanning electron microscopy (SEM, Quanta 200, FEI). The 10−20 $\mu$m thick section of Yunnan pine was also examined through a Nikon biological microscope image analyzer (CELIPSE 80i, Nikon, Japan), and a Leica slicer (SM2000R, Leica, Buffalo Grove) was applied for cutting purposes. X-ray diffraction spectroscopy (XRD, Rigaku, D8 Advance, Bruker) was utilized to determine the crystal structures of the untreated specimens and microfibrillated materials. This was performed using a Rigaku D8 Advance instrument equipped with a nickel-filtered copper Ka−ray ($\lambda$ = 1.5418 Å), 2° min $^{-1}$, current 40 mA, voltage 40 kV, characterized 5−60°. The surface and chemical components of the untreated specimens and microfibrillated materials were analyzed by FT−IR (FTIR, Nicolet iN10 MX) and XPS (XPS, Thermo ESCALAB 250XI). The physical and mechanical


https://doi.org/10.1021/acsomega.3c05251
ACS Omega 2023, 8, 41458−41468

properties of the untreated specimens and microfibrillated materials were measured in accordance with GB11718−2009 by *Shenzhen New Sansi* 50kN microcomputer controlled electronic universal testing machine.

**4.4. Determination of Neutral Detergent Fiber (NDF) in Pure Lignocellulose.** 1.000 g portion of the sample was placed in a cylindrical beaker, and then 100 mL of neutral detergent, several drops of decahydronaphthalene, and 0.5 g of anhydrous sodium sulfite were added. After that, the condensing device on the beaker sleeve was placed in the electric furnace, boiled for 5−10 min, and maintained for 60 min. After this treatment step, the solution and residue in the beaker were all poured into a glass crucible of known weight containing a filter bottle for filtration, and the residue was washed with boiling water until the filtrate was neutral. Afterward, it was washed twice with 20 mL of acetone and filtered. Finally, the glass crucible was placed in a 105 °C oven for 2 h and then cooled in the dryer for 30 min. The mass fraction of neutral detergent fiber in the sample is given by

$$w_{\mathrm{NDF}}(\%) = \frac{m_1 - m_2}{m} \times 100\% \tag{1}$$

where $W_{\mathrm{NDF}}$ is the mass fraction of neutral detergent fiber (%), $m_1$ is the total weight of the glass crucible and NDF, $m_2$ is the weight of the glass crucible, and $m$ is the weight of NDF.

**4.5. Determination of Acid Detergent Fiber (ADF) in Pure Lignocellulose.** 1.000 g portion of the sample was placed in a cylindrical beaker, and then 100 mL of acid detergent, drops of decahydronaphthalene, and 0.5 g of anhydrous sodium sulfite were added. After that, the condensing device on the beaker sleeve was placed on the electric furnace, boiled for 5−10 min, and maintained for 60 min. After this treatment step, the solution and residue in the beaker were all poured into a known-weight glass crucible equipped with a filter bottle for filtration, and the residue was washed with boiling water until the filtrate was neutral. After that, the residue was washed with a small amount of acetone until the acetone solution was colorless, and the acetone was extracted. Finally, the glass crucible was placed in 105 °C ovens for 2 h and then cooled in a dryer for 30 min. The mass fraction of acid detergent fiber in the sample is given by

$$w_{\mathrm{ADF}}(\%) = \frac{m_1 - m_2}{m} \times 100\% \tag{2}$$

where $W_{\mathrm{ADF}}$ is the mass fraction of acid detergent fiber (%), $m_1$ is the total weight of the glass crucible and ADF, $m_2$ is the weight of the glass crucible, and $m$ is the 0 weight of ADF.

**4.6. Determination of Acid Detergent Lignin (ADL) and Acid-Insoluble Ash (AIA) in Pure Lignocellulose.** The acid detergent fiber was added into 5 mL of 72% sulfuric acid at 20 °C for 3 h and then filtered and washed to neutral. After that, the soluble fraction is cellulose, and the insoluble residue is acid-washing lignin and acid-insoluble ash. The content of acid-washed lignin and acid-insoluble ash can be obtained by drying the residue and burning ash. The mass fraction of acid detergent lignin in the sample is given by

$$w_{\mathrm{ADL}}(\%) = \frac{m_1 - m_2 - m_0}{m} \times 100\% \tag{3}$$

where $W_{\mathrm{ADL}}$ is the mass fraction of acid detergent lignin (%), $m_0$ is the weight of 1.000 g pickling asbestos blank value, $m_1$ is the total weight of the glass crucible and ADL, $m_2$ is the weight of ash and glass crucible after ashing, and $m$ is the weight of ADL.

To sum up, we can calculate the content of cellulose/hemicellulose, lignin, and ash in pure lignocellulose according to eqs 1−3.

$$\begin{aligned} W_{\mathrm{CELLULOSE}}(\%) &= \mathrm{ADF}(\%) - \text{residue after72\% sulfuric acid treatment}(\%) \\ W_{\mathrm{HEMICELLULOSE}}(\%) &= \mathrm{NDF}(\%) - \mathrm{ADF}(\%) \\ W_{\mathrm{LIGNIN}}(\%) &= \text{residue after72\%sulfuric acid treatment}(\%) - \text{ash after ashing(silicate, \%)} \\ W_{\mathrm{AIA}}(\%) &= \text{residue after72\%sulfuric acid treatment}(\%) - \mathrm{DL}(\%) \end{aligned} \tag{4}$$

## ■ ASSOCIATED CONTENT

### Supporting Information

The Supporting Information is available free of charge at https://pubs.acs.org/doi/10.1021/acsomega.3c05251.

Additional information, including mechanical properties of the self-cleaning MCCL with other lignocellulosic materials (Table S1) (PDF)

## ■ AUTHOR INFORMATION


### Corresponding Author

**Huajie Shen** − *School of Design, Fujian University of Technology, Fuzhou 350118 Fujian, People's Republic of China;* Present Address: Research and Development Department of Huzhou Boloni Technology Co., Ltd., Huzhou, Zhejiang 313029, People's Republic of China; orcid.org/0000-0002-5462-1262; Email: shenhuajie@fjut.edu.cn

### Authors

**Xinyuan Zheng** − *School of Design, Fujian University of Technology, Fuzhou 350118 Fujian, People's Republic of China*

**Liangzhou Dong** − *School of Design, Fujian University of Technology, Fuzhou 350118 Fujian, People's Republic of China*

**Donghai Huang** − *School of Design, Fujian University of Technology, Fuzhou 350118 Fujian, People's Republic of China*

Complete contact information is available at: https://pubs.acs.org/10.1021/acsomega.3c05251


### Author Contributions

H.S. was the first author who designed and fabricated materials. X.Z., L.D., and D.H. characterized the materials. H.S. wrote the manuscript. H.S. supervised this project.

### Notes

The authors declare no competing financial interest.

## ■ ACKNOWLEDGMENTS

This work was financially supported by the Scientific Research Foundation in Fujian University of Technology (Grant No. GY-Z220296) and Enterprise Scientific Research Project of Huzhou Boloni Technology Co., Ltd (Grant No. 2021ZD01A)

## REFERENCES


(1) Ritter; Geo, J. Composition and Structure of the Cell Wall of wood. *Ind. Eng. Chem.* **1929**, *20* (9), 941−945, DOI: 10.1021/ie50225a020.

(2) Flores, E. S.; Murugan, M.; Friswell, M.; de Souza Neto, E. Computational Multi-Scale Constitutive Model for Wood Cell Wall and Its Application to the Design of Bio-Inspired Composites. In *Bioinspiration, Biomimetics, and Bioreplication*; SPIE, 2011; Vol. *7975*, pp 97−107.

(3) Zhang, X.; Chen, S.; Xu, F. Combining Raman imaging and multivariate analysis to visualize lignin, cellulose, and hemicellulose in the plant cell wall. *J. Visualized Exp.* **2017**, No. 124, No. 55910, DOI: 10.3791/55910.

(4) Dang, B.; Chen, Y.; Shen, X.; Jin, C.; Sun, Q.; Li, X. Fabrication of Fe 3 O 4-modified lignocellulose composite for microwave absorption via a sol−gel-assisted hot-pressing process. *Cellulose* **2019**, *26*, 5455−5466.

(5) Huang, Y.; Wang, Z.; Wang, L.; Chao, Y.; Akiyama, T.; Yokoyama, T.; Matsumoto, Y. Hemicellulose composition in different cell wall fractions obtained using a DMSO/LiCl wood solvent system and enzyme hydrolysis. *J. Wood Chem. Technol.* **2016**, *36* (1), 56−62.

(6) Terashima, N.; Kitano, K.; Kojima, M.; Yoshida, M.; Yamamoto, H.; Westermark, U. Nanostructural assembly of cellulose, hemicellulose, and lignin in the middle layer of secondary wall of ginkgo tracheid. *J. Wood Sci.* **2009**, *55*, 409−416.

(7) O'Neill, M.; Ishii, T.; Albersheim, P.; Darvill, A. Rhamnogalacturonan II: structure and function of a borate cross-linked cell wall pectic polysaccharide. *Annu. Rev. Plant Biol.* **2004**, *55*, 109−139.

(8) Ryden, P.; Sugimoto-Shirasu, K.; Smith, A. C.; Findlay, K.; Reiter, W.; McCann, M. Tensile Properties of Arabidopsis Cell Walls Depend on Both a Xyloglucan Cross-Linked Microfibrillar Network and Rhamnogalacturonan II-Borate Complexes1. *Plant Physiol.* **2003**, *132*, 1033−1040.

(9) Burton, R.; Gidley, M.; Fincher, G. Heterogeneity in the chemistry, structure and function of plant cell walls. *Nat. Chem. Biol.* **2010**, *6*, 724−732.

(10) Yang, Y.; Li, J.; Shan, L.; Qin, L.; Jia, H.; Zheng, P.; Qiu, J. Toughening of high-strength scalable laminated nanocomposites with discontinuous Bouligand-type architecture through soft flow-shear-induced alignment. *Ind. Crops Prod.* **2022**, *189*, No. 115780.

(11) Kinnaert, C.; Daugaard, M.; Nami, F.; Clausen, M. Chemical Synthesis of Oligosaccharides Related to the Cell Walls of Plants and Algae. *Chem. Rev.* **2017**, *117*, 11337−11405.

(12) O'Neill, M.; Eberhard, S.; Albersheim, P.; Darvill, A. Requirement of Borate Cross-Linking of Cell Wall Rhamnogalacturonan II for Arabidopsis Growth. *Science* **2001**, *294*, 846−849.

(13) Soyekwo, F.; Zhang, Q.; Zhen, L.; Ning, L.; Zhu, A.; Liu, Q. Borate crosslinking of polydopamine grafted carbon nanotubes membranes for protein separation. *Chem. Eng. J.* **2018**, *337*, 110−121, DOI: 10.1016/j.cej.2017.12.079.

(14) Chen, Y.; Dang, B.; Jin, C.; Chen, B.; Sun, Q.; Nie, Y. Bio-inspired layered nanolignocellulose/graphene-oxide composite with high mechanical strength due to borate cross-linking. *Ind. Crops Prod.* **2018**, *118*, 65−72.

(15) Wang, Z.; Pan, Q. An Omni-Healable Supercapacitor Integrated in Dynamically Cross-Linked Polymer Networks. *Adv. Funct. Mater.* **2017**, *27*, No. 1700690, DOI: 10.1002/adfm.201700690.

(16) An, Z.; Compton, O.; Putz, K.; Brinson, L.; Nguyen, S. Bio-Inspired Borate Cross-Linking in Ultra-Stiff Graphene Oxide Thin Films. *Adv. Mater.* **2011**, *23*, 3842−3846, DOI: 10.1002/adma.201101544.

(17) Yang, Y.; Li, J.; Shan, L.; Qin, L.; Zheng, P.; Jia, H.; Qiu, J. All-natural bioinspired nanolignocellulose-derived bulk engineering materials with excellent mechanical properties and environmental stability. *Cellulose* **2023**, *30*, 871−884.

(18) Mussana, H.; Yang, X.; Tessima, M.; Han, F.; Iqbal, N.; Liu, L. Preparation of lignocellulose aerogels from cotton stalks in the ionic liquid-based co-solvent system. *Ind. Crops Prod.* **2018**, *113*, 225−233.

(19) Deepa, B.; Abraham, E.; Cordeiro, N.; Mozetič, M.; Mathew, A.; Oksman, K.; Faria, M.; Thomas, S.; Pothan, L. A. Utilization of various lignocellulosic biomass for the production of nanocellulose: a comparative study. *Cellulose* **2015**, *22*, 1075−1090.

(20) Stolarski, M. J.; Krzyżaniak, M.; Łuczyński, M.; Załuski, D.; Szczukowski, S.; Tworkowski, J.; Gołaszewski, J. Lignocellulosic biomass from short rotation woody crops as a feedstock for second-generation bioethanol production. *Ind. Crops Prod.* **2015**, *75*, 66−75.

(21) Cheng, Q.; Duan, J.; Zhang, Q.; Jiang, L. Learning from nature: constructing integrated graphene-based artificial nacre. *ACS Nano* **2015**, *9*, 2231−2234.

(22) Yushan, Y.; Shen, H.; Xian, W.; Qiu, J. Preparation of Nanolignocellulose/Chitin Composites with Superior Mechanical Property and Thermal Stability. *J. Bioresour. Bioprod.* **2019**, *4*, 251−259, DOI: 10.12162/jbb.v4i4.014.

(23) Chen, Y.; Cai, T.; Dang, B.; Wang, H.; Xiong, Y.; Yao, Q.; Wang, C.; Jin, C. Author Correction: The properties of fibreboard based on nanolignocelluloses/CaCO 3 /PMMA composite synthesized through mechano-chemical method. *Sci. Rep.* **2018**, *8*, No. 12633, DOI: 10.1038/s41598-018-30921-9.

(24) Chen, Y.; Dang, B.; Fu, J.; Zhang, J.; Liang, H.; Zhai, T.; Li, H. Bioinspired Construction of Micronano Lignocellulose into an Impact Resistance "Wooden Armor" With Bouligand Structure. *ACS Nano* **2022**, *16*, 7525−7534, DOI: 10.1021/acsnano.1c10725.

(25) Lima, J. S.; Queiroz, J. E. G.; Freitas, H. B. Effect of selected and non-selected urban waste compost on the initial growth of corn. *Resour., Conserv. Recycl.* **2004**, *42*, 309−315, DOI: 10.1016/j.resconrec.2004.02.006.

(26) Zhang, L.; Lu, H.; Yu, J.; McSporran, E.; Khan, A.; Fan, Y.; Yang, Y.; Wang, Z.; Ni, Y. Preparation of High-Strength Sustainable Lignocellulose Gels and Their Applications for Antiultraviolet Weathering and Dye Removal. *ACS Sustainable Chem. Eng.* **2019**, *7*, 2998−3009.

(27) Yang, Y.; Shan, L.; Shen, H.; Qiu, J. Green and Facile Fabrication of Thermal Superamphiphobic Nanofibrillated-cellulose/Chitosan/OTS Composites Through Mechano-Chemical Method. *Fibers Polym.* **2021**, *22*, 1407−1415.




https://doi.org/10.1021/acsomega.3c05251
*ACS Omega* 2023, 8, 41458−41468